

# Preselectable Optical Fingerprints of Heterogeneous Upconversion Nanoparticles

Jiayan Liao, Jiajia Zhou,\* Yiliao Song, Baolei Liu, Yinghui Chen, Fan Wang, Chaohao Chen, Jun Lin, Xueyuan Chen, Jie Lu,\* and Dayong Jin\*



Cite This: *Nano Lett.* 2021, 21, 7659–7668



Read Online

ACCESS |

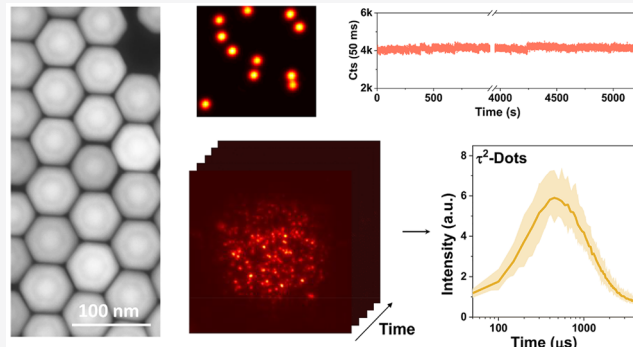
Metrics & More

Article Recommendations

Supporting Information

**ABSTRACT:** The control in optical uniformity of single nanoparticles and tuning their diversity in multiple dimensions, dot to dot, holds the key to unlocking nanoscale applications. Here we report that the entire lifetime profile of the single upconversion nanoparticle ( $\tau^2$  profile) can be resolved by confocal, wide-field, and super-resolution microscopy techniques. The advances in both spatial and temporal resolutions push the limit of optical multiplexing from microscale to nanoscale. We further demonstrate that the time-domain optical fingerprints can be created by utilizing nanophotonic upconversion schemes, including interfacial energy migration, concentration dependency, energy transfer, and isolation of surface quenchers. We exemplify that three multiple dimensions, including the excitation wavelength, emission color, and  $\tau^2$  profile, can be built into the nanoscale derivative  $\tau^2$ -dots. Creating a vast library of individually preselectable nanotags opens up a new horizon for diverse applications, spanning from sub-diffraction-limit data storage to high-throughput single-molecule digital assays and super-resolution imaging.

**KEYWORDS:** *single upconversion nanoparticles, optical fingerprints, multiple dimensions, lifetime profiles*



“**T**here’s Plenty of Room at the Bottom”,<sup>1</sup> and it is the ultimate goal of nanotechnology to manipulate structures with unprecedented accuracy and to tune their functions to precisely match the parameters required at the single-nanoparticle level.<sup>2</sup> Optical multiplexing with increased capacity advances the ongoing development of next-generation enabling technologies, spanning from high-capacity data storage,<sup>3</sup> anticounterfeiting,<sup>4–7</sup> large-volume information communication,<sup>8,9</sup> to high-throughput screening of varied single molecular analytes in a single test,<sup>10,11</sup> and super-resolution imaging of multiple cellular compartments.<sup>12–14</sup>

Supercapacity optical multiplexing challenges our abilities in creating multiplexed codes from the microscopic to the nanoscale and decoding them in a high-throughput fashion with sufficient accuracy.<sup>15,16</sup> When the size of the material that carries the optical barcodes can be pushed to the nanoscopic range, it sacrifices the overall amount of emissive photons (i.e., brightness). Therefore, it limits the number of detectable codes, e.g., typically three to four color channels or brightness levels.<sup>17</sup> The amount of signal from a nanoscale object can drop exponentially, and the size of them is often below the optical diffraction limit, which prevents the conventional filter optics and microscopy techniques from decoding them with sufficient spectral–spatial resolutions. The unmet expectation poses

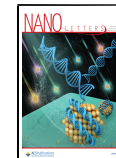
grand challenges for the material sciences to pursue the fabrication strategies and achieve precise control in producing uniform nanoscopic carriers. This further challenges the photonics community to use the limited photon budget of emissive photons to expand the optical diversity (codes), which may be obtained from multiple dimensions, such as emission colors (spectrum),<sup>18,19</sup> lifetime,<sup>20,21</sup> polarization,<sup>22–25</sup> and angular momentum.<sup>26,27</sup> The research focus soon comes to challenge our ability to control the building block of single nanoparticles,<sup>2</sup> to be optically coded with the multidimensional fingerprints.

Lanthanides doped upconversion nanoparticles (UCNPs) can convert the low-energy near-infrared (NIR) photons to emit high-energy emissions in visible and UV regions.<sup>28</sup> Single UCNPs are uniform, photostable for hours, and allow single-nanoparticle tracking experiments in live cells.<sup>29–31</sup> Recently, the core–shell–shell design of each single UCNPs has been reported to emit ~200 photons per second under a low

**Received:** June 22, 2021

**Revised:** August 13, 2021

**Published:** August 18, 2021



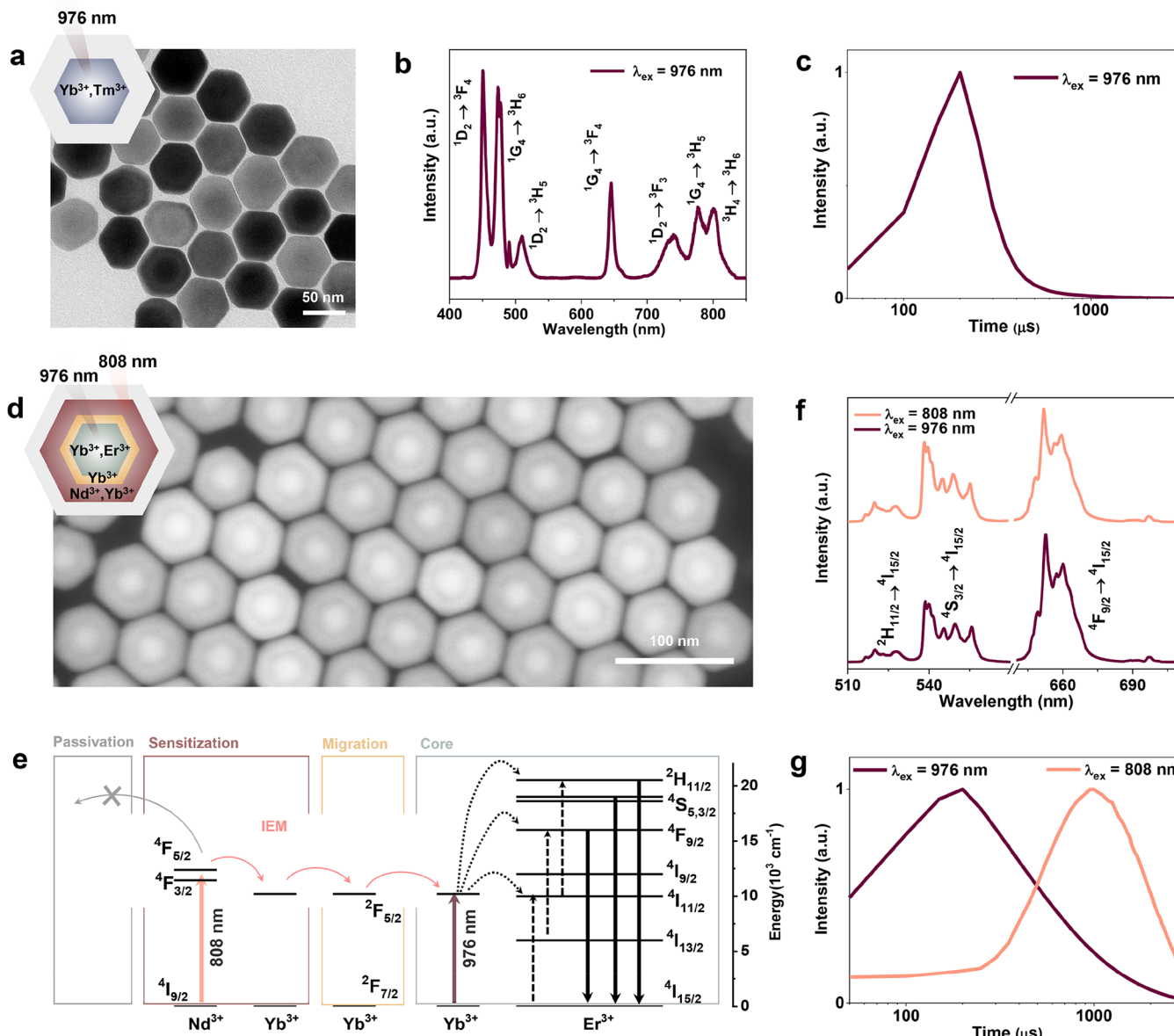


**Figure 1.** Creation of monodisperse UCNPs with optical information in multiple dimensions. (a) TEM image of a kind of typical morphology uniform  $\beta\text{-NaYF}_4$ : $\text{Yb}^{3+}$ ,  $\text{Tm}^{3+}$  core–shell nanoparticles. Scale bar: 50 nm. Ensemble upconversion emission spectrum (b) and lifetime profile (c) of one kind of  $\text{Yb}^{3+}$ ,  $\text{Tm}^{3+}$  doped core–shell UCNPs under 976 nm excitation. (d) HADFF-STEM observation showing the core–multishell structure of the nanoparticles doped with  $\text{Nd}^{3+}$ ,  $\text{Yb}^{3+}$ , and  $\text{Er}^{3+}$  in different layers. Scale bar: 100 nm. (e) Energy level diagram of core–multishell nanoparticles showing the cascade photon energy sensitization, transfer, and conversion process:  $\text{Nd}^{3+}$  ions sensitization at 808 nm,  $\text{Yb}^{3+}$ -mediated interfacial energy migration (IEM) at 976 nm, and upconversion of near-infrared photons into higher-energy visible emissions in a typical  $\text{Yb}^{3+}$ – $\text{Er}^{3+}$  system. Ensemble upconversion emission spectra (f) and lifetime curves (g) of  $\text{Nd}^{3+}$ ,  $\text{Yb}^{3+}$ ,  $\text{Er}^{3+}$  doped core–multishell UCNPs under 808 and 976 nm excitations.

irradiance of  $8 \text{ W/cm}^2$ <sup>32</sup> and intensity uniform UCNPs have enabled the single-molecule (digital) immunoassay.<sup>33,34</sup> The color-based multiplexing of UCNPs can be realized by tuning the dopants,<sup>35–37</sup> core–shell structure,<sup>38,39</sup> or excitation pulse durations.<sup>40</sup> However, all of the color-based approaches are intrinsically limited by the cross-talks in the spectrum domain. In our previous work, we tuned the exceptional long lifetimes of UCNPs in a microsecond-to-millisecond range for multiplexing applications.<sup>21</sup> Major advances since then have been made in the ensemble lifetime measurements of microsphere arrays,<sup>41</sup> time-domain contrast agents for deep-tissue tumor imaging,<sup>42</sup> and high-security-level anticounterfeiting applications.<sup>43</sup> Though lifetime multiplexing with single-nanoparticle sensitivity was possible, the relatively low brightness and the point scanning

confocal microscopy have significantly limited the readout throughput.

In this work, we first demonstrate that heterogeneous UCNPs, with a rather sophisticated design of active core@energy migration shell@sensitization shell@inert shell, can be synthesized with a high degree of morphology uniformity. We find that each batch of single heterogeneous UCNPs is sufficiently bright and optically uniform, displaying correspondingly characteristic optical signatures in the time domain. Remarkably, not only the decay time of each batch of UCNPs is tunable but also the rising time and peak moment of the excited-state population from a single nanoparticle can be further manipulated by the multi-interfacial energy transfer process and different excitation wavelengths. We emphasize that, by

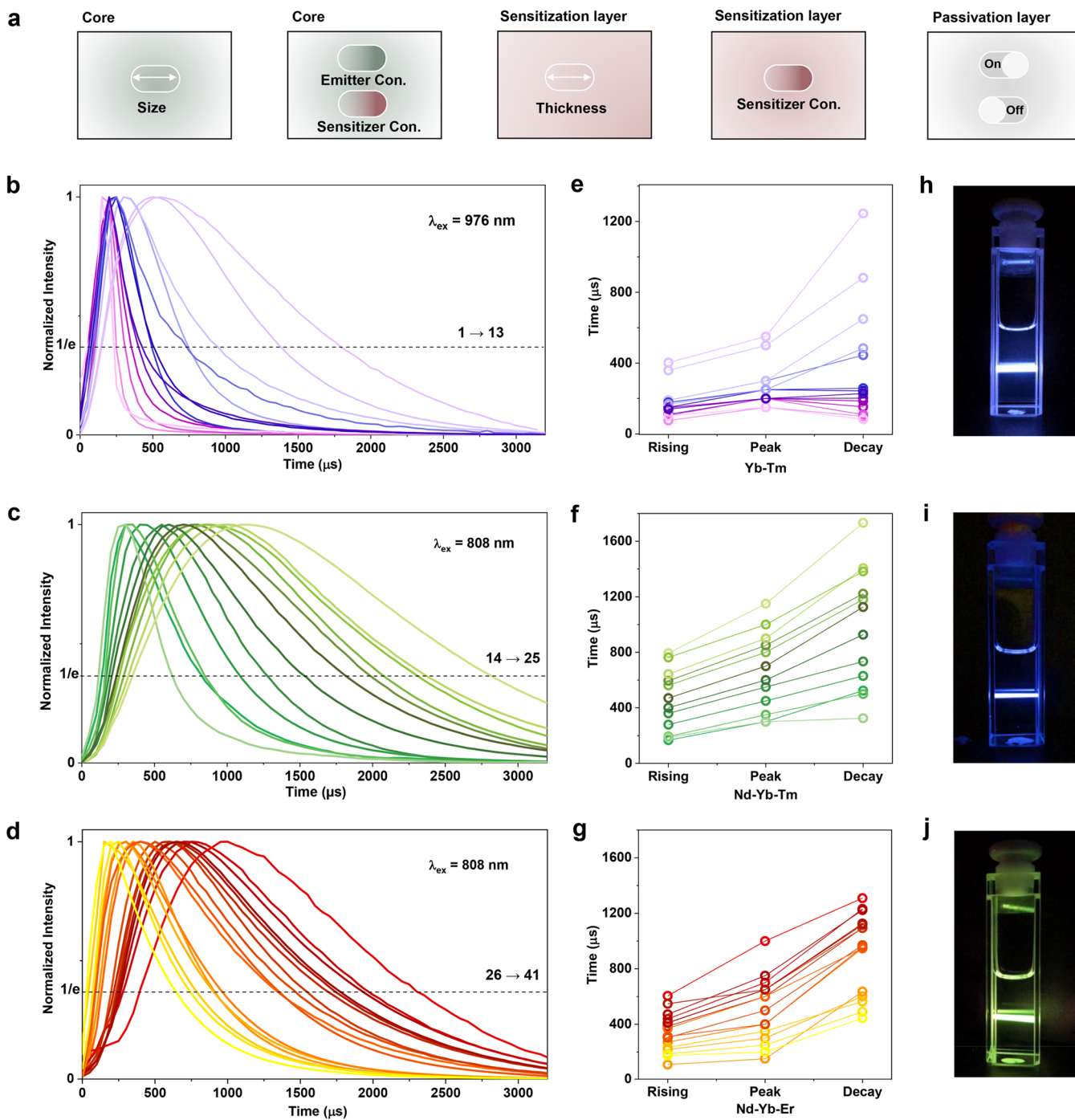


**Figure 2.** Time-domain  $\tau^2$  profiles control through upconversion energy transfer schemes and materials engineering. (a) Illustrations of five strategies used for  $\tau^2$  profiles tuning, i.e., core sizes, the concentrations of sensitizers and emitters in the core, the sensitization layer thickness, the concentration of sensitizers in the sensitization layer, and the passivation layer.  $\tau^2$  profiles tuning of three series of samples, i.e., Yb-Tm series (b), Nd-Yb-Tm series (c), and Nd-Yb-Er series (d), under NIR excitation. Dotted lines indicate the normalized intensity of  $1/e$  ( $I_{1/e}$ ). Calculated rising time ( $\tau_{I_1/I_{1/e},\text{rising}}$ ), peak moment ( $\tau_{I_1}$ ), and decay time ( $\tau_{I_1/I_{1/e},\text{decay}} - \tau_{I_1}$ ) according to the curves in panels b–d for Yb-Tm series (e), Nd-Yb-Tm series (f), and Nd-Yb-Er series (g). Photographs of representative UCNPs in Yb-Tm series (h), Nd-Yb-Tm series (i), and Nd-Yb-Er series (j) showing their upconversion colors under NIR excitation.

controlled synthesis, each batch of UCNPs exhibits a unique set of optical signatures in multiple dimensions, including varied excitation wavelengths, emission colors, and lifetime profiles. The interior features in these dimensions, e.g., the rising time and peak moment of a lifetime profile, are also beneficial to distinguish one batch from another. These high-dimensional optical signatures can be preselected to build a vast library of

single-particle tags. This finding provides a new opportunity for supercapacity multiplexing that integrates multiple dimensions of signals from single nanoparticles.

## RESULTS AND DISCUSSION

**$\tau^2$  Profile.** Three typical series of UCNPs have been investigated in this work (Supporting Information Table S1),

displaying three multiple dimensions (excitation wavelength, emission wavelength, and lifetime profile) of optical fingerprints. The Yb–Tm series (Figure 1a–c) can be excited at 976 nm excitation, the Nd–Yb–Er series (Figure 1d–g), and the Nd–Yb–Tm series (Figure S1) allow both 976 and 808 nm laser excitations.

### Lifetime Engineering of Yb–Tm Series at 976 nm Excitation.

The TEM images in Figure 1a and Figure S2 show the uniform hexagonal  $\beta$ -NaYF<sub>4</sub>: Yb<sup>3+</sup>, Tm<sup>3+</sup> core@inert shell nanoparticles (coefficients of variation (CV) < 5%). Upon excitation of 976 nm, the nanoparticles emit in blue, red, and near-infrared spectral bands, which are assigned to the diverse transitions of Tm<sup>3+</sup> (Figure 1b). All of these excited states (<sup>1</sup>G<sub>4</sub>, <sup>1</sup>D<sub>2</sub>, and <sup>3</sup>H<sub>4</sub>) exhibit both rising, plateau, and decay components in a profile on a microsecond time scale upon pulsed excitation (Figure 1c). This profile renders each different batch of nanoparticles a unique optical fingerprint, featured by a sophisticated multicomponent lifetime behavior, namely,  $\tau^2$  profile. The rising time of the  $\tau^2$  profile is due to the energy transfer from the sensitizers to the activators, which could be characterized using the energy transfer rate. The decay time results from the carrier's relaxation in the excited energy levels. When Yb<sup>3+</sup> ions transfer the pumping energy to the ground state of Tm<sup>3+</sup> ions, the new distribution will be built from the ground state to the excited state of Tm<sup>3+</sup> level by level. The decay time of emission would be achieved by the spontaneous radiation of photons from the excited state.

**Role of Interfacial Energy Migration in Lifetime Engineering.** The  $\tau^2$  concept can be further extended by making a series of core–multishell  $\beta$ -NaYF<sub>4</sub>, Nd<sup>3+</sup>, Yb<sup>3+</sup>, Tm<sup>3+</sup> UCNPs (Figures S3 and S4), and  $\beta$ -NaYF<sub>4</sub>, Nd<sup>3+</sup>, Yb<sup>3+</sup>, Er<sup>3+</sup> UCNPs (Figure 1d and Figure S5), with a great degree of morphology uniformity (CV < 5%). The heterogeneous design of core–multishell UCNPs permits an arbitrary control in the energy transfer process within a single nanoparticle.<sup>44</sup> As illustrated in Figure 1e, the shell co-doped with Nd<sup>3+</sup> and Yb<sup>3+</sup> ions is sensitized upon 808 nm excitation; the energy migration shell containing a small percentage of Yb<sup>3+</sup> ions is responsible for passing on the absorbed energy to the conventional Yb<sup>3+</sup>, Er<sup>3+</sup> co-doped core, which achieves upconverted emissions at the green and red bands (see Figure 1f); an inert shell is employed to prevent the energy migration to the surface quenchers<sup>45,46</sup> and improve the optical uniformity of single nanoparticles. Consequently, there is more time for the excitation energy to migrate through the multilayers nanocrystal, increasing the probability of interfacial energy migration (IEM) to the emitters in the core. The multiple shells can significantly slow down the process of IEM from primary sensitizer Nd<sup>3+</sup> to the secondary sensitizer Yb<sup>3+</sup> under the excitation of 808 nm. IEM plays an important role in the slow accumulation of the excited-state populations, displayed as a time-delayed uprising curve of upconversion emissions. To verify the IEM effect, we selectively excite the Yb<sup>3+</sup> and Nd<sup>3+</sup> ions using 976 and 808 nm lasers, respectively, and observe the same emission spectra (Figure 1f), but many differences in the  $\tau^2$  profiles (Figure 1g). Remarkably, in our demonstration, the rising time for the Er<sup>3+</sup> excited-state populations to reach its plateau can be prolonged nearly 5-fold from 200 to 950  $\mu$ s when the IEM process is involved.

**Multiple Optical Fingerprints Encoding.** On the basis of the above successes in both the controlled synthesis of heterogeneous UCNPs and time-domain tuning of their optical properties, we further implemented five strategies to tailor the excited-state populations of emitters (Tm<sup>3+</sup> and Er<sup>3+</sup>), so a large

set of time-domain optical fingerprints could be created and a library of different batches of  $\tau^2$ -dots built. As illustrated in Figure 2a, the strategies include the tuning of the core size, doping concentrations of emitters and sensitizers in the core, the thickness of the core/sensitization layers, and the doping concentration of Yb<sup>3+</sup> ions in the sensitization layer, as well as the adding of a passivation inert layer. Using these five strategies (Table S1), 13 (1→13 in Figure 2b), 12 (14→25 in Figure 2c), and 16 (26→41 in Figure 2d) batches of three series of  $\tau^2$ -dots have been synthesized in this work. The total of 41 batches of arbitrary design and controlled synthesis resulted in finely tunable  $\tau^2$  profiles under NIR excitation at 976 or 808 nm.

For demonstration purpose, we chose to synthesize two to three representative batches of  $\tau^2$ -dots of Nd–Yb–Er series by each strategy, resulting in a total of over 10 batches of  $\tau^2$ -dot derivatives produced and characterized. As the result of the fast and presumably nonradiative recombination from increasing crystalline defect density, such as vibration energy of surface ligands, solvent quenching, and surface defects,<sup>47,48</sup> the observed lifetime decreases when reducing the nanoparticle size. Because the deposition of the inert shell over the core nanoparticles can mitigate the surface effect responsible for the size-dependent lifetime, and also address the loss in brightness, hence the tunable effect of lifetime curves from different core sizes is not that obvious in the UCNPs of core–inert shell structure (see compared lifetime curves in Figure S6; 36 and 37). Due to the facilitated energy transfer process from Yb<sup>3+</sup> to Er<sup>3+</sup> and cross-relaxation among Er<sup>3+</sup> ions, the lifetimes diminish as the concentrations of Er<sup>3+</sup> or Yb<sup>3+</sup> in the core increase (Figure S7a; Er<sup>3+</sup> doping concentrations in core layer, 33 vs 37). For a transient state, the pulse excitation energy to activate Nd<sup>3+</sup> requires a relatively long path through Yb<sup>3+</sup> to reach activators in the core, which modifies the energy transfer from the activated shell to the core at varied sensitizer–emitter distances and provides further lifetime tunability. It provides an opportunity in that the thickness and doping concentration before self-quenching could also affect the population in the activated state of sensitizers and activators. Hence, the thick sensitization layer (see lifetime curves in Figure S7b, 37 vs 39) or low doped concentration in the sensitization layer (Figure S7c, 37 vs 40 vs 41) both could prolong the rising time of the  $\tau^2$  profiles.

Note here the inert layer can provide surface passivation and reduce the de-excitation effect from the surface quenchers and therefore lengthen the lifetime. Because of this,  $\tau^2$  profiles of passivated dots shift to 2 times longer of the peak moment for different Er<sup>3+</sup> doped concentrations (Figure S8; see lifetime curves 30 vs 37 and 26 vs 33), reaching the peak moments of nearly 650  $\mu$ s for the 2% Er<sup>3+</sup> doped  $\tau^2$ -dots and 400  $\mu$ s for 8% Er<sup>3+</sup> doped  $\tau^2$ -dots. Furthermore, the lifetime tuning of the batches without the inert layer is at the expense of the brightness of single nanoparticles (Figure S9), suggesting that the increased luminescence is due to improved quantum yields for core–shell nanoparticles. Therefore, the nanoparticles with the inert shell were used for the following single-nanoparticle experiments. In conclusion, our results suggest that the surface defects are the primary source of the nonradiative relaxation for the energy dissipation, and the  $\tau^2$ -dots samples with passivated shell protection exhibit longer  $\tau^2$  profiles than the corresponding non-inert shell ones, which is in agreement with the previous reports.<sup>49</sup> For the  $\tau^2$  profiles tuning of passivated  $\tau^2$ -dots are not limited by surface quenching but more likely by internal volume effects in the nanocrystal, such as doping level, thickness, or crystal defects. The vast combinations of different strategies

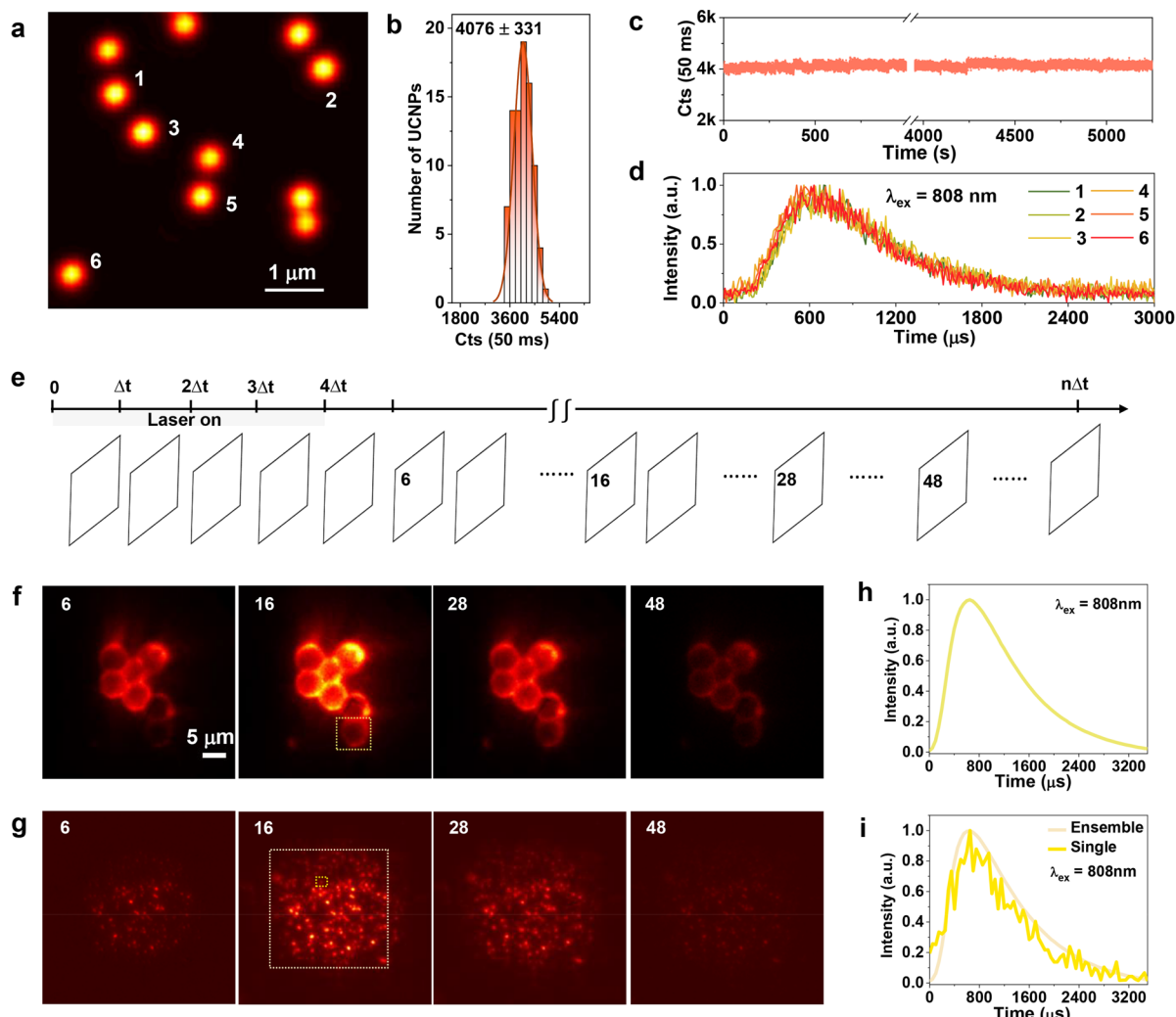


**Figure 3.** Confocal and wide-field characterization of  $\tau^2$ -dots. Confocal microscopic single-nanoparticles imaging (a), brightness distribution (b), long-term photostability of a single dot (c) under 808 nm CW excitation at  $5.5 \times 10^6 \text{ W/cm}^2$ , and corresponding lifetime curves (d) of single dots 1–6 in panel a under 808 nm pulse excitation (by modulating the CW laser at  $5.46 \text{ kW/cm}^2$ ). (e) Schematic illustration of the transient fluorescence signal detection principle using a time-resolved sCMOS camera for wide-field microscopy. Comparison of the time-resolved 6th, 16th, 28th, and 48th frames of  $\tau^2$ -dots-stained micropolystyrene beads (f) and single  $\tau^2$ -dot (g) within a beam area of  $28 \mu\text{m}$  in diameter. (h) Lifetime curve of a single  $\tau^2$ -dots-stained bead, which is indicated by a dotted square in panel f. (i) Normalized lifetime curves of a single and ensemble of  $\tau^2$ -dots, which are indicated by yellow and dark orange dotted squares in panel g. All of the data associate with a random batch of  $\tau^2$ -dot ( $\tau^2$ -12).

enable precise manipulating of the energy transfer process in the  $\tau^2$ -dots, thereby allowing the  $\tau^2$  profiles to be controlled within a wide range.

Though samples from the same doping series exhibit very similar emission colors, i.e., blue for the Yb–Tm series (Figure 2h), violetish blue for the Nd–Yb–Tm series (Figure 2i), and yellowish green for the Nd–Yb–Er series (Figure 2j). An extensive range of lifetime expansions has been achieved in which tens of unique codes can be potentially generated in the same color channel, which extends the multiplexing capacity of UCNPs and offers new opportunities for their applications. Values in Figure 2e–g further quantitatively map the large dynamic ranges of rising time, peak moment, and decay time distributions in identifying each batch of  $\tau^2$ -dots samples.

**Optical Uniformity of Single  $\tau^2$ -Dots.** Despite the large dynamic ranges of lifetime profiles encoded in different batches of  $\tau^2$ -dots, the difference between each encoded optical fingerprint can be hidden at the ensemble measurement level. Therefore, the single-nanoparticle spectroscopy method has to

be adopted to verify the optical uniformity of single  $\tau^2$ -dots. Here, 14 batches of  $\tau^2$ -dots (namely,  $\tau^2$ -1 to  $\tau^2$ -14 in Table S2) in the Yb–Tm series ( $\tau^2$ -1 to  $\tau^2$ -9) and the Nd–Yb–Er ( $\tau^2$ -10 to  $\tau^2$ -14) are tested in the decoding experiment at single-nanoparticle level. Using a confocal microscopy setup (Figure S10), the single-nanoparticle optical characterization results (Figure 3a,b) show a high degree of brightness (e.g., 81,520 photon counts/s for  $\tau^2$ -12 at  $5.46 \times 10^6 \text{ W/cm}^2$ ), and optical uniformity (CV of 8.1%; also see the optical uniformity results by characterizing the nine batches of Nd–Yb–Er  $\tau^2$ -dots in Figure S11). Their exceptional stability of single  $\tau^2$ -dots (Figure 3c) is ideal for long-term imaging and decoding of the optical fingerprints. As shown in Figure 3d, the unique and detectable fingerprint has been successfully assigned to every single  $\tau^2$ -dot. More impressively, the characteristic lifetime fingerprints of single dots from the same synthesis batch are consistently uniform.

**Advances in High-Throughput Time-Resolved Microscopy.** Confocal scanning microscopy allows illumination power

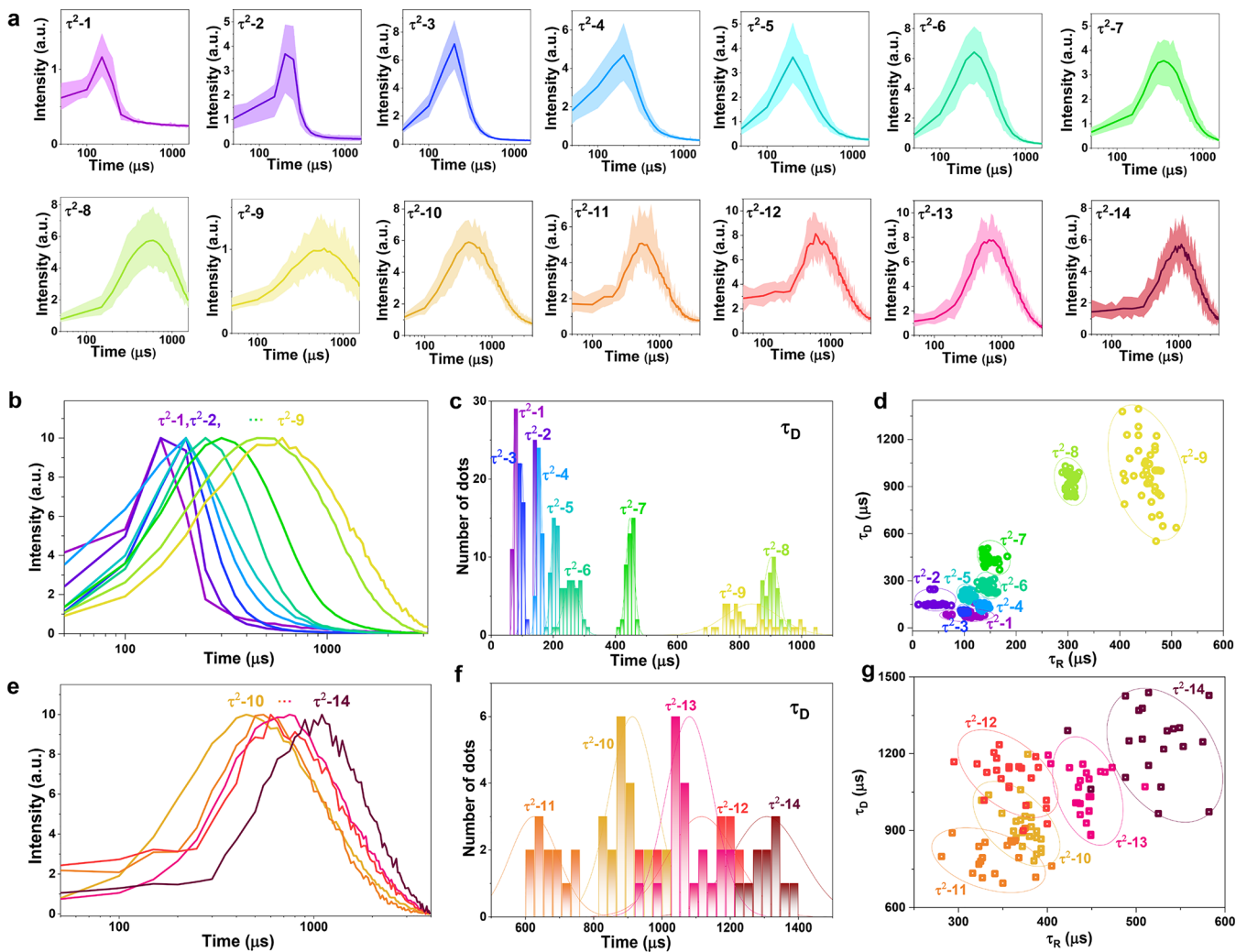


**Figure 4.** Time-domain optical fingerprints from 14 batches of  $\tau^2$ -dots. (a) Lifetime curve statistics from the single  $\tau^2$ -dots. Shaded areas cover the lifetime curves of more than 20 single dots from each type of  $\tau^2$ -dots. The solid colorful lines represent the averaged lifetime curves for each type of  $\tau^2$ -dots. (b and e) Normalized intensity display of averaged single-nanoparticle lifetime fingerprints of Yb-Tm series (nine)  $\tau^2$ -dots and Nd-Yb-Er series (five)  $\tau^2$ -dots. (c and f) Histograms of single-particle decay indicator ( $\tau_D$ ) distribution analysis for the nine batches of Yb-Tm samples  $\tau^2$ -1 to  $\tau^2$ -9 (c) and the four batches of Nd-Yb-Er samples  $\tau^2$ -10 to  $\tau^2$ -14 (f). (d and g) Scatter plots of decay and rising indicators ( $\tau_D$  and  $\tau_R$ ) of samples  $\tau^2$ -1 to  $\tau^2$ -9 (d) and  $\tau^2$ -10 to  $\tau^2$ -14 (g). Because the curve from single  $\tau^2$ -dot has some significant level of noise and fluctuation, the decay ( $\tau_D = \tau_{I_{1/e\_decay}} - \tau_{I_i}$ ) and rising ( $\tau_R = \tau_{I_i} - \tau_{I_{1/e\_rising}}$ ) indicators are roughly calculated as the time interval between the maximum intensity and  $1/e$  of the maximum intensity according to the curves in the panels.

up to  $10^6$  W/cm<sup>2</sup> to excite every single nanoparticle by scanning across each pixel, but of which the scanning mode dramatically limits the throughput in the decoding process. We thus developed the wide-field microscope with an intensifier coupled CMOS camera for time-resolved imaging (Figure S12). While moderate continuous-wave excitation power density (5.46 kW/cm<sup>2</sup>) sacrifices the brightness of each  $\tau^2$ -dot by nearly 2 orders of magnitude (Figure S13), the wide-field setup enhances the decoding throughput by orders of magnitude, compared with the point scanning confocal setup. As shown in Figure 3e, the sequences of time-resolved imaging consist of 75 frames ( $n = 75$ ), which was collected from the time-gated window period ( $\Delta t$ ) of 50  $\mu$ s. By applying the Kinetic Series Mode of the camera and Integrate-On-Chip (IOC) at 250 Hz, we acquired the lifetime image sequences of 75 frames from 0 to 3750  $\mu$ s with a time gate of 50  $\mu$ s under the 200  $\mu$ s pulse laser excitation. By repeating 3000 times of pulse number to accumulate the photon

budget from single nanoparticles, the IOC mode enabled an improved signal-to-noise ratio with a reliable value of around 6.

**Opportunity and Challenge in Using Nanoscale Optical Multiplexing of Single  $\tau^2$ -Dots.** Comparing to the conventional micrometer-sized beads, optical codes created on nanoscopic-sized  $\tau^2$ -dots can significantly increase the capacity of coding information, which takes optical supercapacity multiplexing into the region smaller than the optical diffraction limit. To illustrate the opportunity and challenge, we stained 5  $\mu$ m polystyrene beads with  $\tau^2$ -12 dots (Figure S14) and collected their time-resolved upconversion images. While within an illumination area of 28  $\mu$ m in diameter, a typical image only contains less than 10  $\mu$ m-sized beads (Figure 3f); there are hundreds of single  $\tau^2$ -12 dots presented within the same area of view (Figure 3g). The challenge, however, lies in the dramatically reduced signal strength, as the curve from a single  $\tau^2$ -dot (Figure 3i) has some significant level of noise, due to the limited amount of detectable signal within each 50  $\mu$ s-timed

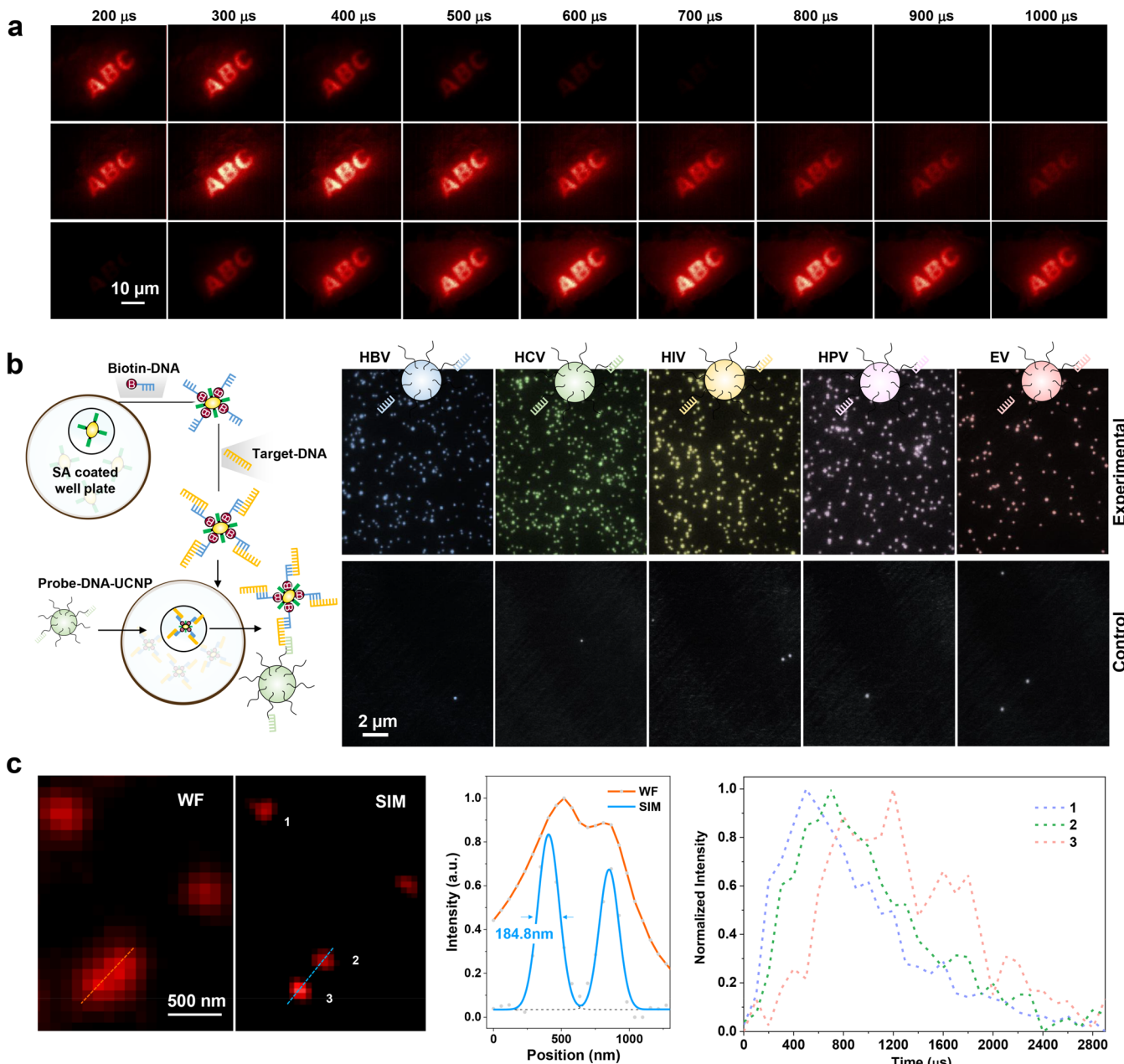


**Figure 5.** Demonstration of the potentials of using the library of single  $\tau^2$ -dots' optical fingerprints for a diverse range of applications. (a) Time-domain anticounterfeiting by using three types of Nd-Yb-Tm series  $\tau^2$ -dots security inks with different rising-decay fingerprints. (b) Multiplexed single-molecule digital assays using five types of Nd-Yb-Er series  $\tau^2$ -dots probes to quantify the five kinds of target pathogen single-stranded DNAs (HBV, HCV, HIV, HPV-16, and EV). Cartoon illustration showing the probe-DNA conjugation procedure on a 96 well plate. (c) Three types of Nd-Yb-Er series  $\tau^2$ -dots resolved by upconversion structure illumination microscopy (U-SIM). Excitation power density is 5.46 kW/cm<sup>2</sup>.

window, while the micrometer bead shows a smooth  $\tau^2$  profile (Figure 3h). The statistic counting of their brightness (see confocal microscopy images in Figure S11) shows that once being properly protected by the passivation layer, all of the derivative populations of  $\tau^2$ -dots provide sufficient photon counts. As shown in Figure S15, over 4000 counts/s for  $\tau^2$ -12 was observed under 808 nm laser excitation at 5.46 kW/cm<sup>2</sup>, which corresponded to the sCMOS camera readout of 8000 under our testing conditions.

**Lifetime Uniformity of Single  $\tau^2$ -Dots.** It is worth noting that, even using the dilute conditions during the sample preparation for single-nanoparticle measurements, it is inevitable for the presence of a small fraction of aggregates (Figure

S15a). We collected the lifetime curves only from single dots, which may be compromised in ensemble measurements. We further measured these 14 batches' lifetime curves of more than 20 single  $\tau^2$ -dots from each batch and presented their lifetime profiles in Figure 4a. We used the sequences of time-dependent frames of images as the source for lifetime profiles extraction of single nanoparticles. (correlated SEM and optical image for single-nanoparticle confirmation in Figure S16). Though some detectable variations of the lifetime curves from dot to dot, caused by the illumination distribution due to Gaussian beam profile of excitation laser (see simulated excitation field in Figure S17) and thereby the power-dependent emission intensities on the excitation irradiance (Figure S18), distinctive characteristics

of each  $\tau^2$ -dot and their lifetime tunability over a large dynamic range are clear (Figure 4b,e). The observed variations of lifetime profiles, from one dot to another, may arise from the doping distributions or subtle variations in the internal defects within the nanocrystal, which poses the challenge for the absolute control of single-nanoparticle growth, while the uniformity of excitation illumination will also contribute to the optical uniformity of the decoding process, suggesting additional scopes for the future improvements.

**Role of High Dimensional Features of Lifetime Fingerprint Profiles.** We can see from Figure 4c,f four pairs of  $\tau^2$ -dots populations, including  $\tau^2\text{-}1$  vs  $\tau^2\text{-}3$ ,  $\tau^2\text{-}2$  vs  $\tau^2\text{-}4$ ,  $\tau^2\text{-}8$  vs  $\tau^2\text{-}9$ , and  $\tau^2\text{-}12$  vs  $\tau^2\text{-}13$ , show significant overlapping. Strikingly, by adding one more indicator, extracted from the lifetime fingerprint profile, i.e.,  $\tau_R$ , the two pairs of populations ( $\tau^2\text{-}2$  vs  $\tau^2\text{-}4$ ,  $\tau^2\text{-}8$  vs  $\tau^2\text{-}9$ ) could be well distinguished (Figure 4d). The remaining pairs remain too challenging to be separated even with the two features  $\tau_D$  and  $\tau_R$  (Figure 4d,g). These indicate that more high-dimensional features are needed to be extracted from the lifetime profile. The potential use of machine learning and new algorithms may help to extract these additional features.

**Potential Diverse Applications Using  $\tau^2$ -Dots.** The nanoscale supercapacity optical multiplexing opens a new horizon for many applications. Using the time-domain  $\tau^2$  profiles, different batches of materials emitting the same color can be used to develop the new generation of dynamic anticounterfeiting security inks, as illustrated in Figure 5a. Another unparalleled potential is to use nanoscale supercapacity multiplexing for high-throughput single molecular assay, which is superior to conventional suspension array assays based on microspheres. As a result of a proof of the principle experiment, in Figure 5b, we designed and functionalized (see Methods in the Supporting Information) the five kinds of  $\tau^2$ -Dots to simultaneously detect the five species of pathogenetic DNA sequences (see DNA sequences in Table S3 and statistical significance in Figure S19). The positive signals of the experimental groups were significantly higher than the control groups, which indicated that there was no nonspecific binding onto the assay plate. The selected DNA sequences are disease-originated, including hepatitis B virus (HBV), hepatitis C virus (HCV), human immunodeficiency virus (HIV), human papillomavirus type-16 (HPV-16), and Ebola virus (EV). Through a wide-field microscope, and compared with the control groups, we concluded that each  $\tau^2$ -dots was highly specific and characteristic. Moreover, as shown in Figure 5c, we demonstrated that the wide-field images of two close  $\tau^2$ -dots with different lifetime profiles could be super-resolved using our latest development of upconversion structure-illumination microscopy (U-SIM)<sup>50</sup> with a resolution of 184.8 nm (1/4th of the 808 nm excitation wavelength), enabling time-resolved super-resolution multiplexing with subdiffraction limit.

## CONCLUSION

In conclusion, we realized the high throughput and high optical dimensions of multiplexing with single-nanoparticle sensitivity. This is based on using the heterogeneous core–multishell design and controlled synthesis of bright and optically uniform UCNPs. Experimentally, we implemented five strategies to tailor the excited-state populations of  $\text{Tm}^{3+}$  and  $\text{Er}^{3+}$  and achieved the single nanoparticles with tunable lifetimes in a wide range. By controlling the energy transfer process, we have produced a total of 41 batches of nanoparticles and demonstrated the arbitrarily tuning of the time-domain  $\tau^2$  profiles for each batch sample. We

have further developed wide-field imaging to decode these multiple optical fingerprints (excitation wavelength, emission color, and  $\tau^2$  profile) from single  $\tau^2$ -dots in high throughput. Comparing to our previous work that uses the averaged decay time of UCNP-decorated microspheres for multiplexing,<sup>41</sup> the use of  $\tau^2$  profiles from the single nanoparticles provides high-dimensional features at the nanoscale. The encoding capacity will meet future demands of high-throughput screening and super-resolution imaging of thousands of single-molecule analytes in a single test.

## ASSOCIATED CONTENT

### Supporting Information

The Supporting Information is available free of charge at <https://pubs.acs.org/doi/10.1021/acs.nanolett.1c02404>.

Details about material synthesis and characterization, optical systems setup, and experimental methods; (Tables S1 and S2) nanoparticle compositions and sizes; (Table S3) pathogenetic DNA sequences; (Figures S1–S5) materials characterizations (TEM images); (Figures S6–S19) optical characterizations (lifetime curves, confocal microscopy images, power-dependent curves) (PDF)

## AUTHOR INFORMATION

### Corresponding Authors

Jiajia Zhou – Institute for Biomedical Materials and Devices (IBMD), Faculty of Science, University of Technology Sydney, Sydney, New South Wales 2007, Australia;  [orcid.org/0000-0002-0605-5745](https://orcid.org/0000-0002-0605-5745); Email: [jiajia.zhou@uts.edu.au](mailto:jiajia.zhou@uts.edu.au)

Jie Lu – Centre for Artificial Intelligence, Faculty of Engineering and IT, University of Technology Sydney, Sydney, New South Wales 2007, Australia; Email: [jie.lu@uts.edu.au](mailto:jie.lu@uts.edu.au)

Dayong Jin – Institute for Biomedical Materials and Devices (IBMD), Faculty of Science, University of Technology Sydney, Sydney, New South Wales 2007, Australia; UTS-SUSTech Joint Research Centre for Biomedical Materials & Devices, Department of Biomedical Engineering, Southern University of Science and Technology, Shenzhen, People's Republic of China;  [orcid.org/0000-0003-1046-2666](https://orcid.org/0000-0003-1046-2666); Email: [dayong.jin@uts.edu.au](mailto:dayong.jin@uts.edu.au)

### Authors

Jiayan Liao – Institute for Biomedical Materials and Devices (IBMD), Faculty of Science, University of Technology Sydney, Sydney, New South Wales 2007, Australia;  [orcid.org/0000-0002-0902-5381](https://orcid.org/0000-0002-0902-5381)

Yiliao Song – Centre for Artificial Intelligence, Faculty of Engineering and IT, University of Technology Sydney, Sydney, New South Wales 2007, Australia

Baolei Liu – Institute for Biomedical Materials and Devices (IBMD), Faculty of Science, University of Technology Sydney, Sydney, New South Wales 2007, Australia

Yinghui Chen – Institute for Biomedical Materials and Devices (IBMD), Faculty of Science, University of Technology Sydney, Sydney, New South Wales 2007, Australia;  [orcid.org/0000-0002-7886-7144](https://orcid.org/0000-0002-7886-7144)

Fan Wang – Institute for Biomedical Materials and Devices (IBMD), Faculty of Science, University of Technology Sydney, Sydney, New South Wales 2007, Australia

Chaohao Chen – Institute for Biomedical Materials and Devices (IBMD), Faculty of Science, University of Technology Sydney, Sydney, New South Wales 2007, Australia

**Jun Lin** — State Key Laboratory of Rare Earth Resource Utilization, Changchun Institute of Applied Chemistry, Chinese Academy of Sciences, Changchun 130022, People's Republic of China;  [orcid.org/0000-0001-9572-2134](https://orcid.org/0000-0001-9572-2134)

**Xueyuan Chen** — CAS Key Laboratory of Design and Assembly of Functional Nanostructures and Fujian Key Laboratory of Nanomaterials, Fujian Institute of Research on the Structure of Matter, Chinese Academy of Sciences, Fuzhou, Fujian 350002, People's Republic of China;  [orcid.org/0000-0003-0493-839X](https://orcid.org/0000-0003-0493-839X)

Complete contact information is available at:  
<https://pubs.acs.org/10.1021/acs.nanolett.1c02404>

### Author Contributions

J.Z. and D.J. conceived the project, designed the experiments, and cosupervised the research; J. Liao. conducted the synthesis, characterization, and measurement. J. Liao and B.L. processed the data; J. Liao and Y.C. performed the single-molecule assay; B.L., F.W., and C.C. built the optical system; Y.S., J. Lu, J. Lin, and X.C., edited the manuscript; J. Liao and J.Z. prepared the figures and Supporting Information; J. Liao. J.Z., and D.J. wrote the manuscript with input from other authors.

### Notes

The authors declare no competing financial interest.

### ACKNOWLEDGMENTS

We acknowledge the financial support from the Australian Research Council Discovery Early Career Researcher Award Scheme (to J.Z., Grant No. DE180100669), China Scholarship Council Scholarships (to J. Liao, Grant No. 201508530231; to B.L., Grant No. 201706020170; to C.C., Grant No. 201607950009), Australia-China Joint Research Centre for Point-of-Care Testing (Grant Nos. ACSRF65827 and 2017YFE0132300), the Science and Technology Innovation Commission of Shenzhen (Grant No. KQTD20170810110913065), the Science and Technology Innovation Commission of Shenzhen (Grant No. 20200925174735005), the CAS/SAFEA International Partnership Program for Creative Research Teams, the National Natural Science Foundation of China (Grant No. 61729501), and the Major International (Regional) Joint Research Project of NSFC (Grant No. 51720105015).

### REFERENCES

- (1) Feynman, R. P. There's Plenty of Room at the Bottom. *Eng. Sci.* **1960**, *23*, 22–36.
- (2) Zhou, J.; Chizhik, A. I.; Chu, S.; Jin, D. Single-Particle Spectroscopy for Functional Nanomaterials. *Nature* **2020**, *579* (7797), 41–50.
- (3) Zhang, Q.; Xia, Z.; Cheng, Y. B.; Gu, M. High-Capacity Optical Long Data Memory Based on Enhanced Young's Modulus in Nanoplasmonic Hybrid Glass Composites. *Nat. Commun.* **2018**, *9* (1), 1183.
- (4) Zhao, J.; Jin, D.; Schartner, E. P.; Lu, Y.; Liu, Y.; Zvyagin, A. V.; Zhang, L.; Dawes, J. M.; Xi, P.; Piper, J. A.; Goldys, E. M.; Monroe, T. M. Single-Nanocrystal Sensitivity Achieved by Enhanced Upconversion Luminescence. *Nat. Nanotechnol.* **2013**, *8* (10), 729–734.
- (5) Li, X.; Guo, Z.; Zhao, T.; Lu, Y.; Zhou, L.; Zhao, D.; Zhang, F. Filtration Shell Mediated Power Density Independent Orthogonal Excitations-Emissions Upconversion Luminescence. *Angew. Chem.* **2016**, *128* (7), 2510–2515.
- (6) Zhou, J.; Wen, S.; Liao, J.; Clarke, C.; Tawfik, S. A.; Ren, W.; Mi, C.; Wang, F.; Jin, D. Activation of the Surface Dark-Layer to Enhance Upconversion in a Thermal Field. *Nat. Photonics* **2018**, *12* (3), 154.
- (7) You, W.; Tu, D.; Li, R.; Zheng, W.; Chen, X. Chameleon-like" Optical Behavior of Lanthanide-Doped Fluoride Nanoplates for Multilevel Anti-Counterfeiting Applications. *Nano Res.* **2019**, *12* (6), 1417–1422.
- (8) Zhang, X.; Yang, S.; Zhou, H.; Liang, J.; Liu, H.; Xia, H.; Zhu, X.; Jiang, Y.; Zhang, Q.; Hu, W.; et al. Perovskite–Erbium Silicate Nanosheet Hybrid Waveguide Photodetectors at the Near-Infrared Telecommunication Band. *Adv. Mater.* **2017**, *29* (21), 1604431.
- (9) Zhou, J.; Leaño, J. L.; Liu, Z.; Jin, D.; Wong, K.; Liu, R.; Bünzli, J. G. Impact of Lanthanide Nanomaterials on Photonic Devices and Smart Applications. *Small* **2018**, *14* (40), 1801882.
- (10) Liu, Q.; Wang, X.; Xia, T. Creative Use of Analytical Techniques and High-Throughput Technology to Facilitate Safety Assessment of Engineered Nanomaterials. *Anal. Bioanal. Chem.* **2018**, *410* (24), 6097–6111.
- (11) Han, M.; Gao, X.; Su, J. Z.; Nie, S. Quantum-Dot-Tagged Microbeads for Multiplexed Optical Coding of Biomolecules. *Nat. Biotechnol.* **2001**, *19* (7), 631–635.
- (12) Klevanski, M.; Herrmannsdoerfer, F.; Sass, S.; Venkataramani, V.; Heilemann, M.; Kuner, T. Automated Highly Multiplexed Super-resolution Imaging of Protein Nano-architecture in Cells and Tissues. *Nat. Commun.* **2020**, *11* (1), 1552.
- (13) Sigal, Y. M.; Zhou, R.; Zhuang, X. Visualizing and Discovering Cellular Structures with Super-Resolution Microscopy. *Science* **2018**, *361* (6405), 880–887.
- (14) Jin, D.; Xi, P.; Wang, B.; Zhang, L.; Enderlein, J.; Van Oijen, A. M. Nanoparticles for Super-Resolution Microscopy and Single-Molecule Tracking. *Nat. Methods* **2018**, *15* (6), 415–423.
- (15) Lin, G.; Baker, M. A. B.; Hong, M.; Jin, D. The Quest for Optical Multiplexing in Bio-Discoveries. *Chem.* **2018**, *4* (5), 997–1021.
- (16) Dong, H.; Sun, L. D.; Feng, W.; Gu, Y.; Li, F.; Yan, C. H. Versatile Spectral and Lifetime Multiplexing Nanoplatform with Excitation Orthogonalized Upconversion Luminescence. *ACS Nano* **2017**, *11* (3), 3289–3297.
- (17) Li, Y.; Cu, Y. T. H.; Luo, D. Multiplexed Detection of Pathogen DNA with DNA-Based Fluorescence Nanobarcodes. *Nat. Biotechnol.* **2005**, *23* (7), 885–889.
- (18) Zhang, Y.; Zhang, L.; Deng, R.; Tian, J.; Zong, Y.; Jin, D.; Liu, X. Multicolor Barcoding in a Single Upconversion Crystal. *J. Am. Chem. Soc.* **2014**, *136* (13), 4893–4896.
- (19) Duan, X.; Kamin, S.; Liu, N. Dynamic Plasmonic Colour Display. *Nat. Commun.* **2017**, *8* (1), 14606.
- (20) Oleksiiews, N.; Thiele, J. C.; Weber, A.; Gregor, I.; Nevskyi, O.; Isbaner, S.; Tsukanov, R.; Enderlein, J. Wide-Field Fluorescence Lifetime Imaging of Single Molecules. *J. Phys. Chem. A* **2020**, *124* (17), 3494–3500.
- (21) Lu, Y.; Zhao, J.; Zhang, R.; Liu, Y.; Liu, D.; Goldys, E. M.; Yang, X.; Xi, P.; Sunna, A.; Lu, J.; Shi, Y.; Leif, R. C.; Huo, Y.; Shen, J.; Piper, J. A.; Robinson, J. P.; Jin, D. Tunable Lifetime Multiplexing Using Luminescent Nanocrystals. *Nat. Photonics* **2014**, *8* (1), 32–36.
- (22) McLellan, J. M.; Li, Z.-Y.; Siekkinen, A. R.; Xia, Y. The SERS Activity of a Supported Ag Nanocube Strongly Depends on Its Orientation Relative to Laser Polarization. *Nano Lett.* **2007**, *7* (4), 1013–1017.
- (23) Grubisic, A.; Ringe, E.; Cobley, C. M.; Xia, Y.; Marks, L. D.; Van Duyne, R. P.; Nesbitt, D. J. Plasmonic Near-Electric Field Enhancement Effects in Ultrafast Photoelectron Emission: Correlated Spatial and Laser Polarization Microscopy Studies of Individual Ag Nanocubes. *Nano Lett.* **2012**, *12* (9), 4823–4829.
- (24) Zhou, J.; Chen, G.; Wu, E.; Bi, G.; Wu, B.; Teng, Y.; Zhou, S.; Qiu, J. Ultrasensitive Polarized Up-Conversion of  $Tm^{3+}$ - $Yb^{3+}$  Doped  $\beta$ -NaYF<sub>4</sub> Single Nanorod. *Nano Lett.* **2013**, *13* (5), 2241–2246.
- (25) Zang, X.; Dong, F.; Yue, F.; Zhang, C.; Xu, L.; Song, Z.; Chen, M.; Chen, P. Y.; Buller, G. S.; Zhu, Y.; Zhuang, S.; Chu, W.; Zhang, S.; Chen, X. Polarization Encoded Color Image Embedded in a Dielectric Metasurface. *Adv. Mater.* **2018**, *30* (21), 1707499.
- (26) Ren, H.; Li, X.; Zhang, Q.; Gu, M. On-Chip Noninterference Angular Momentum Multiplexing of Broadband Light. *Science* **2016**, *352* (6287), 805–809.

- (27) Fang, X.; Ren, H.; Gu, M. Orbital Angular Momentum Holography for High-Security Encryption. *Nat. Photonics* **2020**, *14* (2), 102–108.
- (28) Zhou, B.; Shi, B.; Jin, D.; Liu, X. Controlling Upconversion Nanocrystals for Emerging Applications. *Nat. Nanotechnol.* **2015**, *10* (11), 924–936.
- (29) Wang, F.; Wen, S.; He, H.; Wang, B.; Zhou, Z.; Shimon, O.; Jin, D. Microscopic Inspection and Tracking of Single Upconversion Nanoparticles in Living Cells. *Light: Sci. Appl.* **2018**, *7* (4), 18007.
- (30) Nam, S. H.; Bae, Y. M.; Park, Y. Il; Kim, J. H.; Kim, H. M.; Choi, J. S.; Lee, K. T.; Hyeon, T.; Suh, Y. D. Long-Term Real-Time Tracking of Lanthanide Ion Doped Upconverting Nanoparticles in Living Cells. *Angew. Chem., Int. Ed.* **2011**, *50* (27), 6093–6097.
- (31) Shin, K.; Song, Y. H.; Goh, Y.; Lee, K. T. Two-Dimensional and Three-Dimensional Single Particle Tracking of Upconverting Nanoparticles in Living Cells. *Int. J. Mol. Sci.* **2019**, *20* (6), 1424.
- (32) Liu, Q.; Zhang, Y.; Peng, C. S.; Yang, T.; Joubert, L. M.; Chu, S. Single Upconversion Nanoparticle Imaging at Sub-10 W  $\text{cm}^{-2}$  Irradiance. *Nat. Photonics* **2018**, *12* (9), 548–553.
- (33) He, H.; Liu, B.; Wen, S.; Liao, J.; Lin, G.; Zhou, J.; Jin, D. Quantitative Lateral Flow Strip Sensor Using Highly Doped Upconversion Nanoparticles. *Anal. Chem.* **2018**, *90* (21), 12356–12360.
- (34) Farka, Z.; Mickert, M. J.; Hlaváček, A.; Skládal, P.; Gorris, H. H. Single Molecule Upconversion-Linked Immunosorbent Assay with Extended Dynamic Range for the Sensitive Detection of Diagnostic Biomarkers. *Anal. Chem.* **2017**, *89* (21), 11825–11830.
- (35) Zhang, F.; Shi, Q.; Zhang, Y.; Shi, Y.; Ding, K.; Zhao, D.; Stucky, G. D. Fluorescence Upconversion Microbarcodes for Multiplexed Biological Detection: Nucleic Acid Encoding. *Adv. Mater.* **2011**, *23* (33), 3775–3779.
- (36) Wu, S.; Duan, N.; Shi, Z.; Fang, C.; Wang, Z. Simultaneous Aptasensor for Multiplex Pathogenic Bacteria Detection Based on Multicolor Upconversion Nanoparticles Labels. *Anal. Chem.* **2014**, *86* (6), 3100–3107.
- (37) Chan, E. M.; Han, G.; Goldberg, J. D.; Gargas, D. J.; Ostrowski, A. D.; Schuck, P. J.; Cohen, B. E.; Milliron, D. J. Combinatorial Discovery of Lanthanide-Doped Nanocrystals with Spectrally Pure Upconverted Emission. *Nano Lett.* **2012**, *12* (7), 3839–3845.
- (38) Dou, Q.; Idris, N. M.; Zhang, Y. Sandwich-Structured Upconversion Nanoparticles with Tunable Color for Multiplexed Cell Labeling. *Biomaterials* **2013**, *34* (6), 1722–1731.
- (39) Wang, F.; Deng, R.; Wang, J.; Wang, Q.; Han, Y.; Zhu, H.; Chen, X.; Liu, X. Tuning Upconversion through Energy Migration in Core–Shell Nanoparticles. *Nat. Mater.* **2011**, *10* (12), 968–973.
- (40) Deng, R.; Qin, F.; Chen, R.; Huang, W.; Hong, M.; Liu, X. Temporal Full-Colour Tuning through Non-Steady-State Upconversion. *Nat. Nanotechnol.* **2015**, *10* (3), 237–242.
- (41) Lu, Y.; Lu, J.; Zhao, J.; Cusido, J.; Raymo, F. M.; Yuan, J.; Yang, S.; Leif, R. C.; Huo, Y.; Piper, J. A.; et al. On-the-Fly Decoding Luminescence Lifetimes in the Microsecond Region for Lanthanide-Encoded Suspension Arrays. *Nat. Commun.* **2014**, *5* (1), 3741.
- (42) Gu, Y.; Guo, Z.; Yuan, W.; Kong, M.; Liu, Y.; Liu, Y.; Gao, Y.; Feng, W.; Wang, F.; Zhou, J.; et al. High-Sensitivity Imaging of Time-Domain near-Infrared Light Transducer. *Nat. Photonics* **2019**, *13* (8), 525–531.
- (43) Ren, W.; Lin, G.; Clarke, C.; Zhou, J.; Jin, D. Optical Nanomaterials and Enabling Technologies for High-security-level Anticounterfeiting. *Adv. Mater.* **2020**, *32* (18), 1901430.
- (44) Liao, J.; Jin, D.; Chen, C.; Li, Y.; Zhou, J. Helix Shape Power-Dependent Properties of Single Upconversion Nanoparticles. *J. Phys. Chem. Lett.* **2020**, *11* (8), 2883–2890.
- (45) Fischer, S.; Bronstein, N. D.; Swabeck, J. K.; Chan, E. M.; Alivisatos, A. P. Precise Tuning of Surface Quenching for Luminescence Enhancement in Core-Shell Lanthanide-Doped Nanocrystals. *Nano Lett.* **2016**, *16* (11), 7241–7247.
- (46) Würth, C.; Fischer, S.; Grauel, B.; Alivisatos, A. P.; Resch-Genger, U. Quantum Yields, Surface Quenching, and Passivation Efficiency for Ultrasmall Core/Shell Upconverting Nanoparticles. *J. Am. Chem. Soc.* **2018**, *140* (14), 4922–4928.
- (47) Zhao, J.; Lu, Z.; Yin, Y.; McRae, C.; Piper, J. A.; Dawes, J. M.; Jin, D.; Goldys, E. M. Upconversion Luminescence with Tunable Lifetime in  $\text{NaYF}_4:\text{Yb},\text{Er}$  Nanocrystals: Role of Nanocrystal Size. *Nanoscale* **2013**, *5* (3), 944–952.
- (48) Gargas, D. J.; Chan, E. M.; Ostrowski, A. D.; Aloni, S.; Altow, M. V. P.; Barnard, E. S.; Sanii, B.; Urban, J. J.; Milliron, D. J.; Cohen, B. E.; Schuck, P. J. Engineering Bright Sub-10-Nm Upconverting Nanocrystals for Single-Molecule Imaging. *Nat. Nanotechnol.* **2014**, *9* (4), 300–305.
- (49) Chen, B.; Wang, F. Combating Concentration Quenching in Upconversion Nanoparticles. *Acc. Chem. Res.* **2020**, *53* (2), 358–367.
- (50) Liu, B.; Chen, C.; Di, X.; Liao, J.; Wen, S.; Su, Q. P.; Shan, X.; Xu, Z.-Q.; Ju, L. A.; Mi, C.; et al. Upconversion Nonlinear Structured Illumination Microscopy. *Nano Lett.* **2020**, *20* (7), 4775–4781.